



Energy-resolved plasmonic chemistry in individual nanoreactors

Eitan Oksenberg¹, Ilan Shlesinger¹, Angelos Xomalis², Andrea Baldi^{3,4}, Jeremy J. Baumberg², A. Femius Koenderink¹ and Erik C. Garnett¹✉

Plasmonic resonances can concentrate light into exceptionally small volumes, which approach the molecular scale. The extreme light confinement provides an advantageous pathway to probe molecules at the surface of plasmonic nanostructures with highly sensitive spectroscopies, such as surface-enhanced Raman scattering. Unavoidable energy losses associated with metals, which are usually seen as a nuisance, carry invaluable information on energy transfer to the adsorbed molecules through the resonance linewidth. We measured a thousand single nanocavities with sharp gap plasmon resonances spanning the red to near-infrared spectral range and used changes in their linewidth, peak energy and surface-enhanced Raman scattering spectra to monitor energy transfer and plasmon-driven chemical reactions at their surface. Using methylene blue as a model system, we measured shifts in the absorption spectrum of molecules following surface adsorption and revealed a rich plasmon-driven reactivity landscape that consists of distinct reaction pathways that occur in separate resonance energy windows.

Plasmonic nanostructures can concentrate light into subnanoscale volumes owing to their unique optical properties^{1,2}. This exceptional ability, along with the relative ease of spectral tunability, have propelled a massive interest in plasmonics for efficient harvesting and conversion of light for optoelectronics, photovoltaics, sensing and, more recently, mediating chemical reactions^{3–5}. At the heart of these applications lie chemical and physical processes that occur at the surface of metallic nanostructures^{6–8}. Characterizing and understanding these processes is essential to realize the great potential that plasmonic applications hold. However, studying interfacial processes is a challenging task both experimentally and theoretically, especially under ambient conditions. As a result, there are still gaps in our understanding of the interplay between plasmonic structures and their chemical environment^{9,10}.

Two such unsettled debates are how the optical absorption of molecules is affected once they are adsorbed on plasmonic nanoparticles¹¹, and what physical process governs plasmon-driven chemistry¹⁰. It is challenging to directly measure the absorbance of metal-bound dye molecules as their absorption cross-section is substantially smaller than that of plasmonic structures. As a result, the absorbance of molecules is frequently assumed to be unchanged, although their electronic structure is often altered once adsorbed onto a metal¹¹. In the case of plasmon-mediated chemistry, the enhanced optical near fields, resulting in high-energy ('hot') charge carriers, and photogenerated heat can all drive chemical reactions at the surface of plasmonic nanostructures (further discussion in Supplementary Section 1)¹⁰. An ongoing debate over which process dominates in plasmon-induced reactions is fuelled by difficulties in experimentally deconvoluting these processes, and the lack of a complete theoretical description^{12–17}. These ambiguities hinder further progress in the field, despite a growing and impressive body of work^{18–24}, and the potential to generate more selective, efficient or even alternative reaction pathways while driving the chemistry under mild conditions^{25–31}.

Here we demonstrate an energy-resolved approach to experimentally study chemical and physical processes at the surface of individual plasmonic nanoparticles. We fabricated plasmonic nanocavities composed of gold nanocubes deposited on a gold mirror coated with a thin dielectric layer (NCoMs)^{2,32}. The enhanced near fields offer a valuable opportunity to study single particles and small populations of molecules (a few hundred to a few thousand molecules per nanocavity) in operando with characterization tools that are extremely sensitive to their chemical environment. We avoided ensemble averaging and harnessed the sharp plasmonic resonances of these nanocavities to track changes in their chemical environment through resonance lineshape analysis. The plasmon lineshape—its energy, intensity and homogeneous linewidth—is extremely sensitive to its chemical environment through chemical interface damping (CID)^{33–40}. By closely monitoring changes in the nanocavity resonance lineshape, we tracked and gained insight into surface processes, such as molecular adsorption and plasmon-driven reactions. Thanks to the enhanced fields, we also performed complementary single-cavity surface-enhanced Raman spectroscopy (SERS) to identify the chemical species that participated in the plasmon-driven reaction. Finally, by slightly varying the NCoM geometry and probing 500 cavities across a 1.6–2.1 eV energy range, we achieved an average sampling distance of ~1 meV between individual resonances. Together, the information gathered from each nanocavity formed an energy-resolved depiction of the plasmonic surface chemistry.

Energy-tunable plasmonic nanoreactors

Our energy-resolved plasmonic platform utilizes the versatile nanoparticle-on-mirror configuration^{3,32}. Gold nanocubes, used for their superior structural stability⁴¹, were separated by a thin Al₂O₃ layer from a gold mirror (nanocube on a mirror (NCoM)), as illustrated in Fig. 1a. Lumerical's finite-difference time-domain (FDTD) calculations were used to extract the near-field profile of an NCoM using a 76 nm rounded-edge nanocube separated from a gold mirror

¹Center for Nanophotonics, AMOLF, Amsterdam, the Netherlands. ²NanoPhotonics Centre, Cavendish Laboratory, Department of Physics, University of Cambridge, Cambridge, UK. ³DIFFER—Dutch Institute for Fundamental Energy Research, Eindhoven, the Netherlands. ⁴Department of Physics and Astronomy, Vrije Universiteit Amsterdam, Amsterdam, the Netherlands. ✉e-mail: e.garnett@amolf.nl

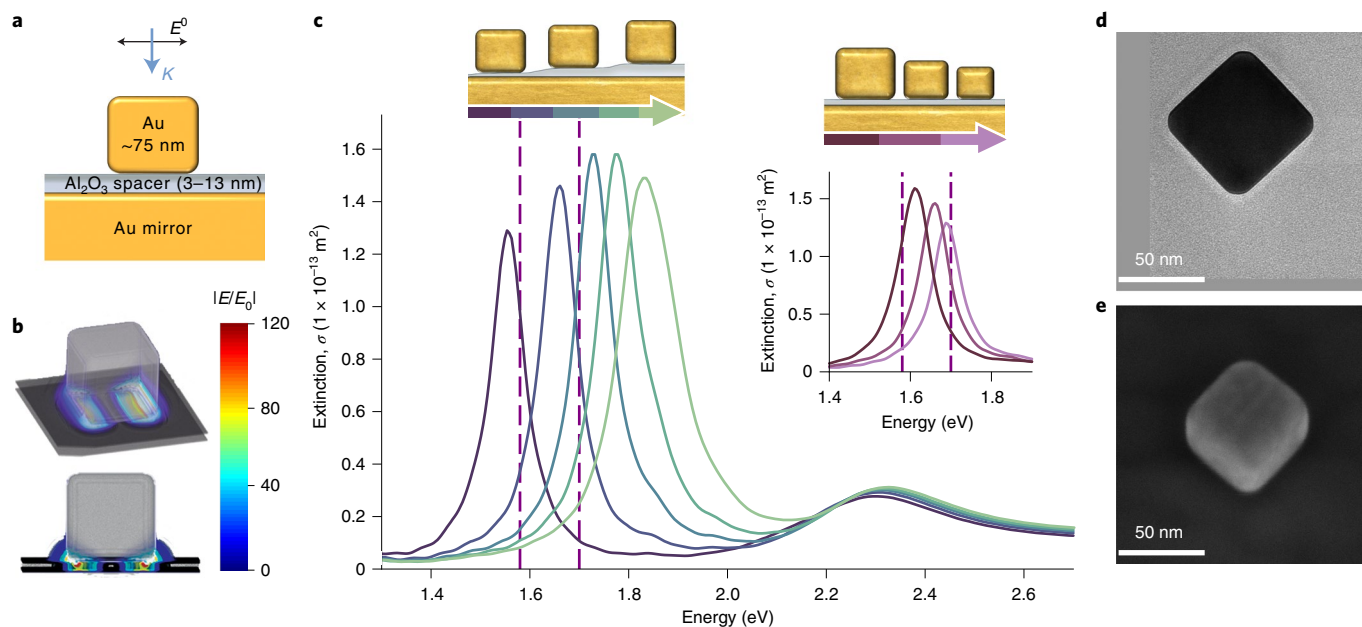


Fig. 1 | NCoMs as energy-tunable nanoreactors. **a**, Illustration of the NCoM configuration. E^0 and K are the electric field amplitude and wavevector of the incident light. **b**, FDTD-simulated three-dimensional (3D) field-enhancement profiles for a 76 nm cube, a dielectric spacer thickness of 10 nm and a normal incidence excitation at the (11) mode (1.73 eV). **c**, Simulated FDTD extinction cross-section (σ) spectra using a 76 nm cube and varying the spacer thickness from 6 to 15 nm (dark-purple to light-green curves). The vertical dashed purple lines indicate a small energy range (inset) in which the resonance energy is tuned by maintaining a constant 8 nm dielectric spacer thickness and varying the nanocube dimension from 79 to 73 nm (dark-purple to pink curves). **d,e**, TEM image of a typical nanocube (**d**) and a tilted SEM image of a fabricated NCoM cavity (**e**).

by a 10 nm Al_2O_3 layer for resonant excitation (1.73 eV) at normal incidence that corresponded to its (11) gap resonance (Fig. 1b)⁴². The studied spectral range, 1.6–2.1 eV (600–780 nm), was chosen to limit gold interband transitions⁴³ and include the methylene blue (MB) electronic transition. To effectively resolve this energy range, we fabricated five samples with varying spacer thicknesses (3, 4, 6, 9 and 13 nm) via atomic layer deposition of thin Al_2O_3 layers on 100-nm-thick gold mirrors. Citrate-capped gold nanocubes with a typical side length of 70–78 nm were dropcast onto these Al_2O_3 -coated mirrors to generate the NCoM geometry. Figure 1c shows how the extinction cross-section spectra are expected to vary with changes in the dielectric spacer thickness and nanocube size (simulation details are given in Methods and Supplementary Section 2). A transmission electron microscope (TEM) image of a typical nanocube and a tilted scanning electron microscope (SEM) image of a characteristic NCoM are shown in Fig. 1d,e.

An illustration of the semi-automated integrating sphere microscopy set-up used to measure the extinction spectra of individual NCoMs is shown in Fig. 2a (detailed descriptions in Methods and Supplementary Section 3). Figure 2b–f depicts a typical measurement scheme. First, a region of interest was imaged with an SEM in low magnification (Fig. 2b), and then the sample was placed on a piezo-stage inside an integrating sphere at the focal distance from a long (17 mm) working-distance objective (numerical aperture (NA) 0.42) to generate a low-resolution extinction map ($\sim 1 \mu\text{m}$ step size) (Fig. 2c). The extinction map was then overlaid on the SEM image (Fig. 2d) to select NCoMs that were well separated from other scatterers. Once an isolated NCoM was found, a higher-resolution ($\sim 350 \text{ nm}$ step size, Fig. 2e inset) spatial scan was performed to place the cavity at the centre of the excitation beam before the stage was fixed. An extinction spectrum was acquired by scanning across the chosen excitation wavelengths with a tunable light source using a supercontinuum laser passed through a computer-controlled acousto-optic tunable filter (AOTF). Figure 2e shows an

experimental extinction spectrum of a typical NCoM with a sharp peak at 1.83 eV, which corresponds to its (11) gap resonance⁴². In Fig. 2f, we schematically illustrate the formation of a resonance energy scale from 12 experimental spectra. For the following sections, each dataset was formed by measuring ~ 500 individual nanocavities separated by $\sim 1 \text{ meV}$. This resonance energy resolution is required to accurately map the chemical and physical processes at the surface of plasmonic nanoparticles.

Effective absorption of adsorbed molecules

The extinction spectra of NCoMs fabricated using citrate-capped gold nanocubes were measured before and after the sample was placed for five hours in a 15 mM aqueous solution of MB to exchange the ligands (details in Methods and Supplementary Section 4). Figure 3a,b shows the homogeneous linewidth (Γ) versus the NCoM gap resonance energy (E_{res}) spanning the 1.6–2.0 eV energy range. The simulated linewidths of NCoMs with bare nanocubes (solid grey line) are shown along with the experimental linewidths of NCoMs with citrate-capped (Fig. 3a) and MB-capped nanocubes (Fig. 3b). Each point in these plots represents the E_{res} and Γ , fitted by a Lorentzian, of a single NCoM experimental extinction spectrum. Mean linewidth (solid coloured line) and its standard deviation (shaded regions) were calculated by dividing the spectral range into 15–20 bins.

The resonances with the adsorbed molecules mostly follow the simulated trend for bare NCoMs, showing the linewidth broadens with increasing resonance energy. Marked deviations from the bare-nanocavities trend, most notably the rise at $\sim 1.9 \text{ eV}$ for MB, indicate the effect of adsorbed molecules on the linewidth. Simulated Γ versus E_{res} trends of NCoMs fully covered with non-absorbing and absorbing thin shells (Supplementary Fig. 4) fail to reproduce the observed changes to the NCoMs linewidths (Fig. 3b). Importantly, FDTD calculations take into account only the optical properties of the absorptive shells. Therefore, the differences between the calculated and the experimental results highlight that

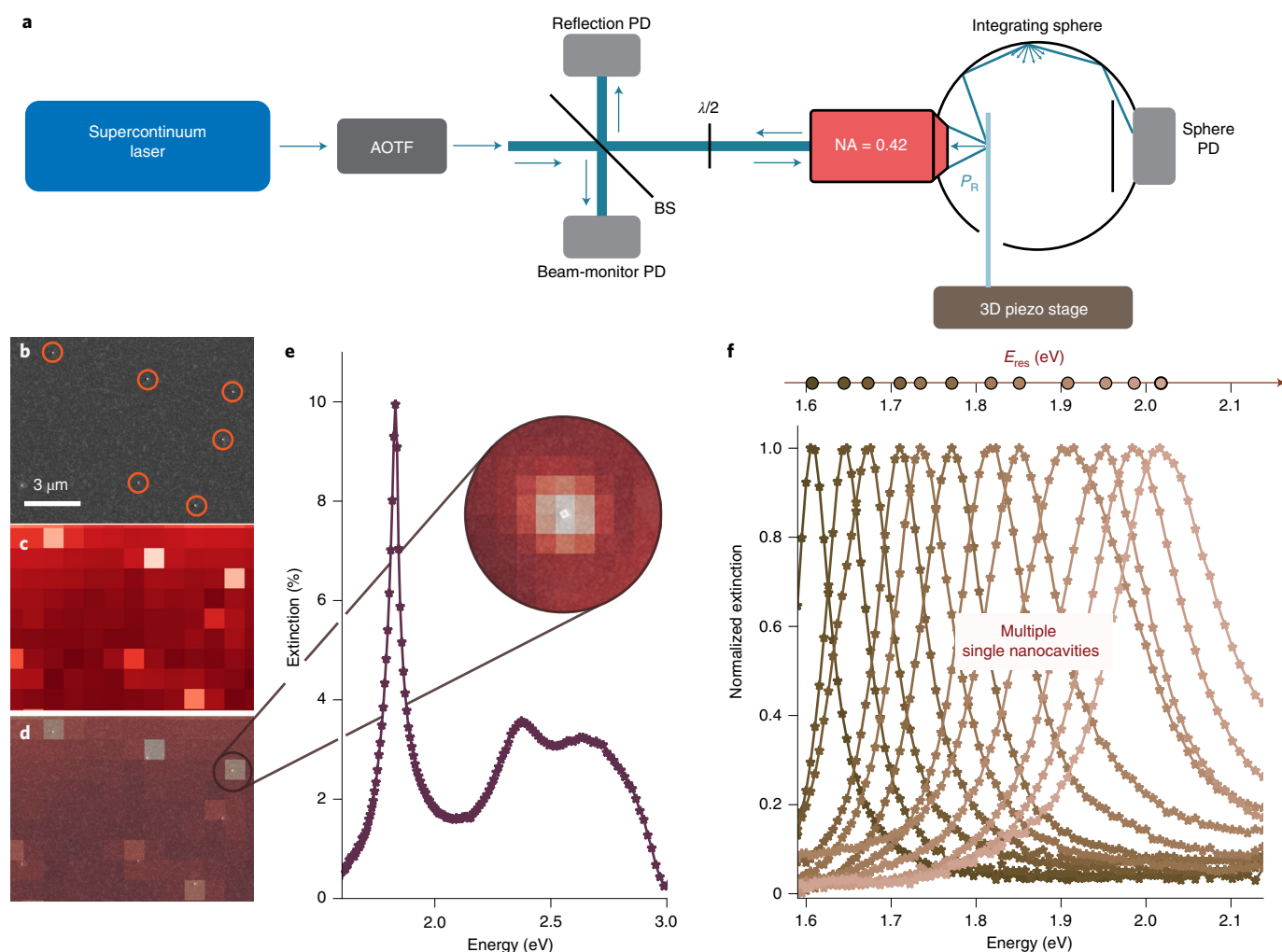


Fig. 2 | Forming an experimental resonance energy scale. **a**, Illustration of the integrating sphere set-up. A supercontinuum laser along with an AOTF are used to select the excitation wavelength. A beam splitter (BS) directs part of the light to the beam monitor photodetector (PD), and the rest goes through a half-wave plate and a long-working-distance objective into the integrating sphere, where the sample is positioned on the 3D piezo-stage. Reflected light (P_R) travels back along the path and is redirected into the reflection PD. **b–d**, Low-magnification SEM image of a region of interest that contains a few NCoMs (highlighted with red circles) (**b**), its corresponding spatially resolved extinction map (**c**) and an overlay of the extinction map and the SEM image (**d**). **e**, Characteristic experimental full extinction spectrum of a single NCoM. Inset: overlay of SEM image of the NCoM and its higher-resolution spatial extinction map. **f**, Schematic illustration of forming a resonance energy scale (E_{res}) from the gap plasmon extinction spectra of 12 selected NCoMs with different spacer thicknesses and cube sizes.

an additional damping process, beyond radiative damping, dominates the experimental observations. We attribute these discrepancies to the strong impact of the NCoM chemical environment on its linewidth through CID^{33–40}.

We used CID-induced lineshape changes to probe modifications to the NCoM chemical environment. Importantly, although the lineshape changes were easily observed, we did not see directly any MB absorption peaks in the obtained extinction spectra (Supplementary Fig. 4). Also, although the ligand exchange reactions are expected to saturate in the conditions used⁴⁴, small variations in the surface coverage, as well as variations in the number and orientation of the molecules adsorbed onto the nanocubes (taking into account the nanocube size distribution) probably contribute to small changes in the extent of the linewidth broadening. These deviations are expected to generate statistical variations (blue-shaded areas), which undermines our ability to accurately calculate the single-molecule CID contribution (Supplementary Section 4).

With MB, the additional contribution to the linewidth around 1.9 eV is especially interesting as its highest occupied molecular

orbital–lowest unoccupied molecular orbital (HOMO–LUMO) electronic transition when dissolved in water is at ~ 1.85 eV (Supplementary Fig. 5). To isolate the CID-induced broadening due to MB adsorption ($\Delta\Gamma_{\text{ads}}$), the simulated linewidth of bare cavities (grey solid line, Fig. 3b) is subtracted from the experimental data for MB adsorbed on NCoMs (solid blue line, Fig. 3b). The resulting adsorption-induced spectrum has a prominent peak at ~ 1.9 eV (Fig. 3c, blue curve), similar to the absorbance of solvated MB in water (grey curve).

CID-induced linewidth broadening is commonly attributed to additional damping channels that reduce the plasmon lifetime due to its chemical environment^{7,33–40}, and recently interfacial molecule–metal states were suggested to have a critical role in these lineshape changes⁴⁵. Previous theoretical predictions directly tie the extent of the linewidth broadening to the degree of overlap between the plasmon resonance energy and the HOMO–LUMO electronic transition of the adsorbed molecules, as well as their spatial and polarization overlap⁴⁶. Following these concepts, characterizing the energy-resolved linewidth broadening induced by

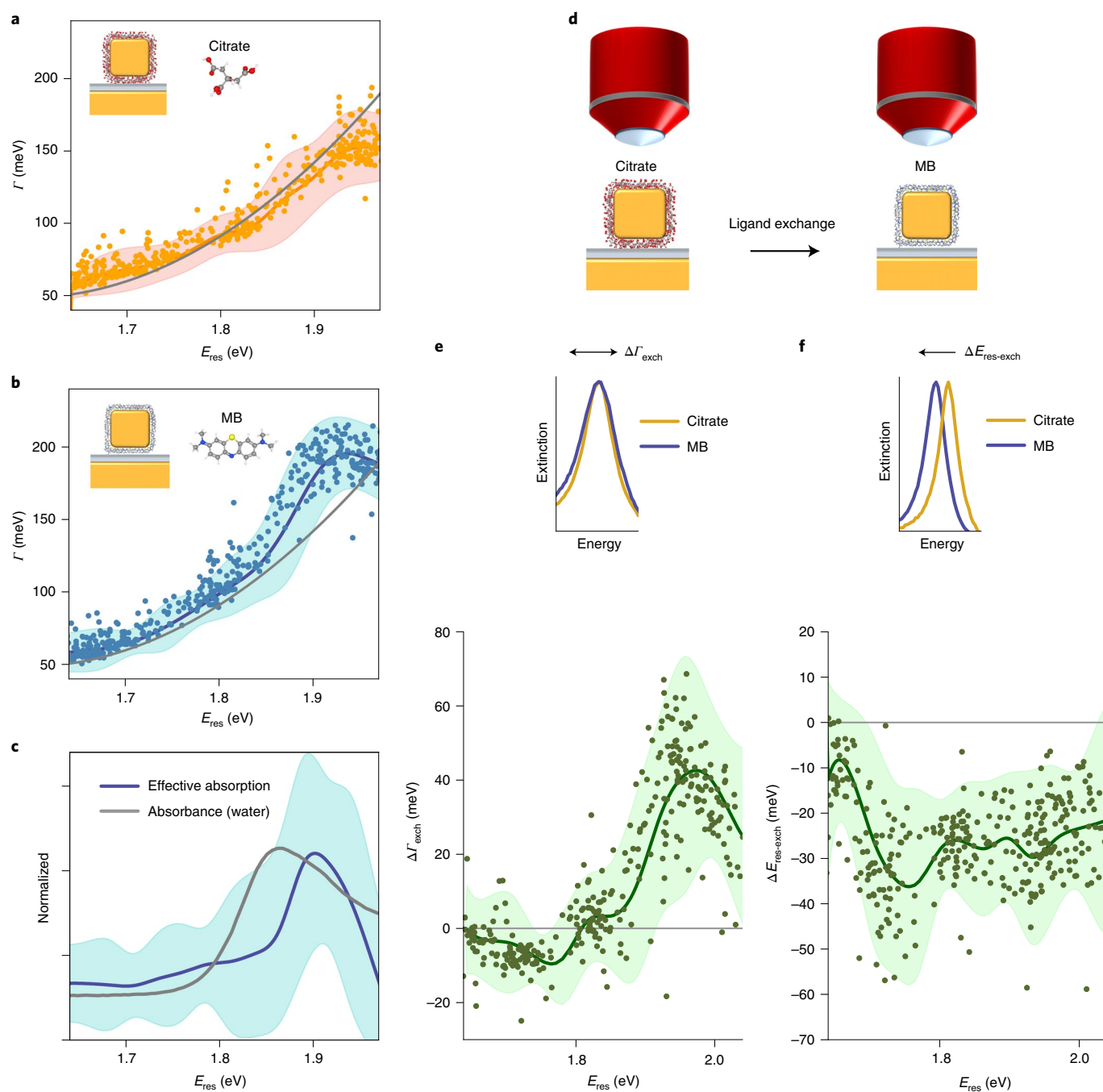


Fig. 3 | CID and effective molecular absorption. a, b, Homogeneous linewidth (Γ) versus gap plasmon resonance energy (E_{res}) measured for single NCoMs with citrate (**a**) and MB (**b**) adsorbed onto the gold nanocubes. Each point represents the centre of a fitted Lorentzian (E_{res}) and its linewidth (Γ) to the measured extinction spectrum of a single NCoM. Mean linewidth (solid coloured lines) and its standard deviation (shaded regions) are calculated by dividing the spectral range into 15–20 bins. The grey line shows the simulated linewidth of bare NCoMs. **c,** Normalized adsorption-induced linewidth broadening due to MB adsorption (blue, shaded regions indicate the standard deviation) and normalized absorbance spectrum of MB in water (grey). **d,** Schematic measurement scheme for **e** and **f**. **e, f,** The extinction spectrum is measured with citrate ligands and, following ligand exchange, a second extinction spectrum is measured using the same cavity, this time with the adsorbed MB ligands. The top panels show the experimental resonance linewidth or energy changes of the chosen cavities to highlight the lineshape changes probed in the plots in the bottom panels. Each point in the plots represents the difference between MB and citrate in linewidth ($\Delta\Gamma_{exch}$) (**e**) and resonance energy ($\Delta E_{res-exch}$) (**f**) for an individual cavity. Means and standard deviations are plotted as solid lines and shaded areas, respectively.

molecular adsorption constitutes an alternative approach to characterize the HOMO–LUMO transition of the metal-bound adsorbate, which effectively determines its absorption spectrum. We thus characterized the effective absorption spectrum of metal-bound molecules after any adsorption-induced electronic structure

changes. The observed ~ 40 meV blueshift compared with the MB absorbance spectrum in water probably results from adsorption induced changes in electronic structure or differences in the refractive index surrounding MB. Additional discussion can be found in Supplementary Section 4. Supplementary Section 7 offers an

additional dataset for 4-nitrothiophenol (NTP), and discussion on the citrate CID-induced features.

To highlight, strictly experimentally, the sensitivity of the resonance lineshape to the adsorbed chemical moieties, we tracked changes in the linewidth and resonance energy of each cavity as the adsorbed ligands are exchanged (Fig. 3d). The resulting differences in linewidths ($\Delta\Gamma_{\text{exch}}$) and resonance energies ($\Delta E_{\text{res-exch}}$) for NCoMs with MB and citrate are summarized in Fig. 3e,f. The mean (solid lines) and its standard deviation (shaded regions) were calculated by binning the energy range into 15–20 bins. After MB adsorption, there was a mild-to-no (0–15 meV) linewidth narrowing (Fig. 3e) in the 1.6–1.85 eV energy range, which is probably due to resonance redshifts following MB adsorption. The strong broadening peak (more than 40 meV) centred at ~1.9 eV is attributed to the overlap between the MB HOMO–LUMO transition and the cavity resonance, as discussed in the previous paragraph. The resonance energy (Fig. 3e) shows an almost spectrally flat ~30 meV redshift, in line with CID-induced redshifts previously observed with thiol ligands^{34,36,38}. An additional NTP dataset can be found in Supplementary Section 7.

Plasmon-driven chemistry in individual nanoreactors

The energy resolution of this platform offers a path to resolve the convoluted contribution of enhanced near-fields, resulting hot carriers and photothermal heating on an energy scale^{10,17}, and also to identify the governing mechanisms that drive the chemistry. To do so, the rate or selectivity of a reaction is probed by varying the energy of the driving plasmonic resonances. In this scenario, we would expect near-field driven reactions and hot charge-carrier-driven reactions to show a substantial rate (or selectivity) enhancement peak when the plasmon energy matches that of the molecular electronic transition⁴⁶ and of a coupled molecule–metal transition²⁰, respectively. Photothermally driven reactions should not show an abrupt increase in the rate or selectivity at specific resonance energies, as similar absorption cross-sections and illumination intensities on similar plasmonic structures would lead to similar photothermal heating when varying the resonance energies across the probed range²⁴.

To gain this energy-resolved perspective, we used the gap resonances of single NCoMs to simultaneously activate and spectroscopically monitor plasmon-driven reactions. Each nanocavity was treated as a single chemical reactor and the adsorbed molecules as chemical reactants. To drive and follow the potential chemical reactions, the evolution of the extinction spectra of each cavity was recorded during ten consecutive wavelength scans. The measurements were conducted first with citrate ligands as the reference. Subsequently, ligand exchange (as described in the previous section) was used to adsorb MB molecules onto the NCoMs, and ten further scans were recorded. Figure 4a,b summarizes the evolution of the resonance lineshape during consecutive scans. Each point shows the difference in resonance linewidths (Fig. 4a) and energies (Fig. 4b) between the tenth and the first scan either with MB adsorbed onto the nanocubes (blue) or only citrate (orange). The mean (solid line) and its standard deviation (shaded regions) were calculated by binning the data into 15–20 bins (see Supplementary Sections 5–7 for further details and additional NTP datasets).

We identified two distinct features indicative of surface processes. The first, at ~1.9 eV, is a prominent minimum in $\Delta\Gamma_{\text{res-act}}$ (blue, Fig. 4a), indicating strong linewidth narrowing. The insets show consecutive extinction spectra (top) of a typical cavity and the evolution of the linewidth (bottom) during the scans. The second feature, at ~1.7 eV, is a noticeable peak in $\Delta E_{\text{res-act}}$ (Fig. 4b), which indicates a substantial blueshift of the NCoM resonance. Again, this is directly seen (inset) in a typical nanocavity, with the extinction spectra (top) and blueshifts (bottom) during scans. Clearly, the signal evolution in both cases changes rapidly during the first scans,

followed by a slower, approaching saturation, behaviour. This exponential trend resembles a first-order chemical reaction and provides an alternative way to track the kinetics within single nanoreactors through the lineshape evolution (a kinetic analysis demonstration is given in Supplementary Section 6). In stark contrast to the noticeable features in the MB curves, the orange citrate curves show no dramatic features.

To unveil the chemical species and underlying chemistry that drives the trends shown in Fig. 4a,b, we targeted cavities with resonance energies that corresponded to the features seen at ~1.9 and ~1.7 eV. We performed SERS measurements on selected single cavities. The measurements were conducted in two different set-ups to resonantly excite the cavities in the two energy regimes using 633 nm (1.96 eV, 22–275 $\mu\text{W}\mu\text{m}^{-2}$) and 770 nm (1.61 eV, 2–44 $\mu\text{W}\mu\text{m}^{-2}$) laser excitations. A typical spectrum from a ~1.9 eV NCoM (Fig. 4c) shows (above a large PL background) a common MB vibration at ~440 cm^{-1} (blue solid line) along with an additional vibration at ~480 cm^{-1} (green dashed line) that is attributed to the *N*-demethylation derivatives of MB, such as thionine¹⁵. SERS spectra from ~1.7 eV NCoMs (Fig. 4d) show no sign of the MB derivative vibrations; however, we observe a strong enhancement in the anti-Stokes peaks that correspond to MB vibrations, especially at about ~440 cm^{-1} (blue arrow), which arises from vibrational pumping. In our system, this vibrational pumping is not driven by elevated temperatures, but suggests a charge-transfer process (see Supplementary Section 5 for further discussion)^{20,47}.

We combined the lineshape analysis and SERS results to gain an energy-resolved perspective of MB plasmon-driven chemistry. We note that each extinction spectrum was obtained by scanning through the whole wavelength range (580–780 nm), and therefore we cannot exclude processes that occur off resonance within that range. However, given our relatively low excitation (~1.4 $\mu\text{W}\mu\text{m}^{-2}$), and based on recent literature on MB plasmonic chemistry^{15,20}, the on-resonance plasmonic processes probably dominate our observations. We also considered only marginal contributions of the gold interband transitions as we did not excite below 580 nm (2.14 eV) (ref. 43).

In the lower resonance energy range (~1.7 eV), driving the plasmon-mediated chemistry resulted in minor (~5 meV) linewidth broadening (Fig. 4a) along with a strong resonance energy blueshift (~15 meV, the positive peak in Fig. 4b). These trends appear to partially reverse the lineshape changes observed after MB adsorption. Simulated extinction spectra of NCoMs with different absorptive shells (Supplementary Fig. 11) indicate that this effect is not caused by changes in the refractive index and absorption of the ligand shell, but is CID-induced after changes to the NCoM chemical environment. The lack of new chemical moieties combined with elevated anti-Stokes peaks and the decrease in the MB SERS signal over time (Supplementary Fig. 8) along with the reversal of the MB adsorption induced lineshape changes points to a desorption process (although we cannot exclude severe fragmentation). A desorption reaction after a charge-transfer process can be expected from consulting decades of research on the fragmentation or desorption of metal-bound molecules as a result of electronic transitions stimulated by high-energy charge carriers or photons^{18,49}. As this process occurs specifically at ~1.7 eV, which does not overlap with the MB electronic transition, we conclude that at this energy we observe a charge-transfer-driven MB desorption, as illustrated in Fig. 4d.

At ~1.9 eV the plasmon-driven chemistry results in a strong linewidth narrowing (~30 meV, negative peak in Fig. 4a). SERS results support an energy-specific chemical transformation, as the signature of *N*-demethylation derivatives of MB was observed only when cavities with this resonance energy were measured. Furthermore, the *N*-demethylation derivative vibrational signal increases over time (Supplementary Fig. 6). We, therefore, conclude that this reaction, which occurs specifically at the MB electronic transition energy, is

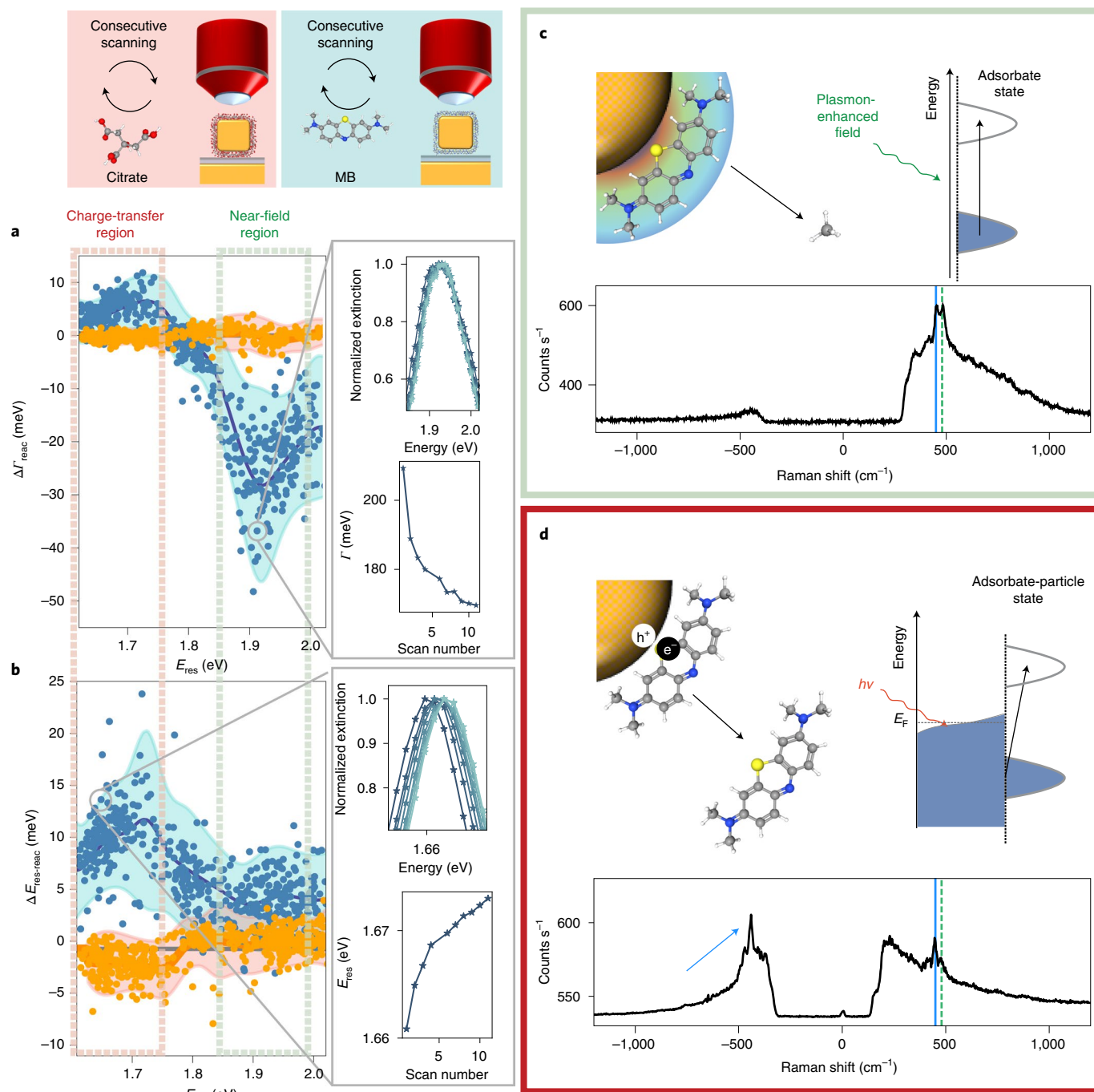


Fig. 4 | MB blue plasmon-driven chemistry. **a, b**, Differences in linewidth (**a**) and resonance energy (**b**) between the tenth and first extinction spectra of single NCoMs with adsorbed MB (blue) or citrate (orange). The means (lines) and standard deviations (shaded areas) are shown. Insets: representative cavities show the measured consecutive extinction spectra (top panels) and the evolution of linewidths (**a**) and resonance energies (**b**) (bottom panels) during ten consecutive scans. The schematic in the top left illustrates the measurement scheme. **c, d**, SERS spectra taken with a 633 nm (1.96 eV) laser ($22 \mu\text{W} \mu\text{m}^{-2}$, 1 s integration, averaged over 30 spectra) (**c**) and with a 770 nm (1.61 eV) laser ($2 \mu\text{W} \mu\text{m}^{-2}$, 1 s integration averaged over 100 spectra) (**d**) along with characteristic vibration bands for MB (solid blue line) and thionine (dashed green line). In **d**, the elevated anti-Stokes of MB is indicated with a blue arrow. Insets: illustrations of plasmon-mediated near-field-driven *N*-demethylation of MB around 1.9 eV (**c**) and charge-transfer-driven desorption of MB, where E_f is the Fermi level (**d**).

a plasmon-mediated *N*-demethylation driven by the enhanced near fields. The strong increase in light intensity at the nanocavity surface increases the probability of electronic excitation, which leads to enhanced chemical transformations. The ~ 30 meV linewidth narrowing is attributed to a reduction in overlap between the electronic transition of the adsorbates and the nanocavity resonance energy

after the chemical reaction, from a maximal overlap with MB (1.86 eV in water) to a reduced overlap with its blueshifted *N*-demethylation derivatives (2.07 eV for thionine in water)¹⁵ (see Supplementary Sections 5–7 for further discussion and additional NTP datasets).

Our analysis reveals that the plasmonic chemistry in this system is governed by enhanced near fields, which results in electronic

excitations; either the excitation of a MB electronic transition at ~ 1.9 eV or the excitation of a coupled MB–gold transition at ~ 1.7 eV. We found no evidence that photothermal effects dictated, in a substantial manner, the underlying chemistry in this system. As charge transfer requires newly formed interfacial molecule–metal states, but near-field driven chemistry does not, one might suggest that the two chemical pathways occur within two different subpopulations of MB—one directly bound to the gold nanocubes and one located in close proximity (that is, multilayers). However, the striking differences between the experimental and simulated trends (Supplementary Figs. 5 and 11) indicate that the experimental results are governed by CID and not by proximity-related radiative damping. As the lineshape analysis is dominated by CID, which probably stems from interfacial molecule–metal–formed states⁴⁵, the changes we observed are the result of processes that occur within the interfacial MB population that forms such states. Therefore, both reaction pathways occur within the same interfacial MB population that is subjected to energy-dependent plasmonic chemistry.

Conclusions

In this work, we have demonstrated an energy-resolved plasmonic tool that can be used to initiate and simultaneously spectroscopically probe chemical and physical processes at the surface of plasmonic nanostructures. The extinction spectral lineshapes of single nanocavities hold valuable information about their chemical environment, while the enhanced near fields are used to identify the participating chemical species through single-cavity SERS. We have demonstrated that the energy-resolved resonance linewidth of nanocavities holds sufficient information to construct effective absorption spectra of metal-bound molecules. Repetitively exciting the cavity resonances can drive plasmon-mediated chemistry and provide information about the kinetics and underlying mechanism of the reaction. We demonstrate how this approach can be used to map the reactivity landscape of MB and unveil that even within a system with minimal chemical participants, a rich landscape can emerge. In fact, within a modest energy range, we observed two distinct chemical processes within the same interfacial MB population: a near-field driven *N*-demethylation and a charge-transfer induced desorption. We saw no evidence that photothermal effects dictated the underlying chemistry in our system, as both reaction pathways were governed by electronic excitations that stem from the enhanced plasmonic near fields. Our findings demonstrate the richness of plasmon-driven chemistry and offer a glimpse at the opportunity to identify spectral windows in which different fundamental mechanisms drive alternative chemical pathways. We envision an even richer reactivity landscape as cavity resonances are shifted into the mid-infrared and overlap with the bond vibrations of adsorbed molecules⁵⁰. Insights from such reactivity maps are extremely valuable for designing plasmonic platforms that support light-driven reactions with a high selectivity and conversion efficiency.

Online content

Any methods, additional references, Nature Research reporting summaries, source data, extended data, supplementary information, acknowledgements, peer review information; details of author contributions and competing interests; and statements of data and code availability are available at <https://doi.org/10.1038/s41565-021-00973-6>.

Received: 15 December 2020; Accepted: 3 August 2021;
Published online: 4 October 2021

References

- Wang, F. & Shen, Y. R. General properties of local plasmons in metal nanostructures. *Phys. Rev. Lett.* **97**, 206806 (2006).
- Baumberg, J. J., Aizpurua, J., Mikkelsen, M. H. & Smith, D. R. Extreme nanophotonics from ultrathin metallic gaps. *Nat. Mater.* **18**, 668–678 (2019).
- Liang, Z., Sun, J., Jiang, Y., Jiang, L. & Chen, X. Plasmonic enhanced optoelectronic devices. *Plasmonics* **9**, 859–866 (2014).
- Atwater, H. A. & Polman, A. Plasmonics for improved photovoltaic devices. *Nat. Mater.* **9**, 205–213 (2010).
- Zhang, Y. et al. Surface-plasmon-driven hot electron photochemistry. *Chem. Rev.* **118**, 2927–2954 (2018).
- Brongersma, M. L., Halas, N. J. & Nordlander, P. Plasmon-induced hot carrier science and technology. *Nat. Nanotechnol.* **10**, 25–34 (2015).
- Haes, A. J., Zou, S., Zhao, J., Schatz, G. C. & Van Duyne, R. P. Localized surface plasmon resonance spectroscopy near molecular resonances. *J. Am. Chem. Soc.* **128**, 10905–10914 (2006).
- Kumar, P. V. et al. Plasmon-induced direct hot-carrier transfer at metal–acceptor interfaces. *ACS Nano* **13**, 3188–3195 (2019).
- Taylor, A. B. & Zijlstra, P. Single-molecule plasmon sensing: current status and future prospects. *ACS Sens.* **2**, 1103–1122 (2017).
- Zhan, C., Moskovits, M. & Tian, Z.-Q. Recent progress and prospects in plasmon-mediated chemical reaction. *Matter* **3**, 42–56 (2020).
- Darby, B. L., Auguie, B., Meyer, M., Pantoja, A. E. & Le Ru, E. C. Modified optical absorption of molecules on metallic nanoparticles at sub-monolayer coverage. *Nat. Photon.* **10**, 40–45 (2016).
- Dubi, Y., Un, I. W. & Sivan, Y. Thermal effects—an alternative mechanism for plasmon-assisted photocatalysis. *Chem. Sci.* **11**, 5017–5027 (2020).
- Yu, S. & Jain, P. K. The chemical potential of plasmonic excitations. *Angew. Chem. Int. Ed.* **59**, 2085–2088 (2020).
- Seemala, B. et al. Plasmon-mediated catalytic O₂ dissociation on Ag nanostructures: hot electrons or near fields? *ACS Energy Lett.* **4**, 1803–1809 (2019).
- Tesema, T. E., Kafle, B. & Habteyes, T. G. Plasmon-driven reaction mechanisms: hot electron transfer versus plasmon-pumped adsorbate excitation. *J. Phys. Chem. C* **123**, 8469–8483 (2019).
- Kamarudheen, R., Aalbers, G. J. W., Hamans, R. F., Kamp, L. P. J. & Baldi, A. Distinguishing among all possible activation mechanisms of a plasmon-driven chemical reaction. *ACS Energy Lett.* **5**, 2605–2613 (2020).
- Baffou, G., Bordacchini, I., Baldi, A. & Quidant, R. Simple experimental procedures to distinguish photothermal from hot-carrier processes in plasmonics. *Light Sci. Appl.* **9**, 108 (2020).
- Kazuma, E., Jung, J., Ueba, H., Trenary, M. & Kim, Y. Real-space and real-time observation of a plasmon-induced chemical reaction of a single molecule. *Science* **360**, 521–526 (2018).
- Brandt, N. C., Keller, E. L. & Frontiera, R. R. Ultrafast surface-enhanced Raman probing of the role of hot electrons in plasmon-driven chemistry. *J. Phys. Chem. Lett.* **7**, 3179–3185 (2016).
- Boerigter, C., Campana, R., Morabito, M. & Linic, S. Evidence and implications of direct charge excitation as the dominant mechanism in plasmon-mediated photocatalysis. *Nat. Commun.* **7**, 10545 (2016).
- Tan, S. et al. Plasmonic coupling at a metal/semiconductor interface. *Nat. Photon.* **11**, 806–812 (2017).
- Hervier, A., Renzas, J. R., Park, J. Y. & Somorjai, G. A. Hydrogen oxidation-driven hot electron flow detected by catalytic nanodiodes. *Nano Lett.* **9**, 3930–3933 (2009).
- Zheng, Z., Tachikawa, T. & Majima, T. Plasmon-enhanced formic acid dehydrogenation using anisotropic Pd–Au nanorods studied at the single-particle level. *J. Am. Chem. Soc.* **137**, 948–957 (2015).
- Jain, P. K. Taking the heat off of plasmonic chemistry. *J. Phys. Chem. C* **123**, 24347–24351 (2019).
- Cortés, E. et al. Plasmonic hot electron transport drives nano-localized chemistry. *Nat. Commun.* **8**, 14880 (2017).
- Zhang, X. et al. Product selectivity in plasmonic photocatalysis for carbon dioxide hydrogenation. *Nat. Commun.* **8**, 14542 (2017).
- Vadai, M., Angell, D. K., Hayee, F., Sytwu, K. & Dionne, J. A. In-situ observation of plasmon-controlled photocatalytic dehydrogenation of individual palladium nanoparticles. *Nat. Commun.* **9**, 4658 (2018).
- Szczerbiński, J., Gyr, L., Kaeslin, J. & Zenobi, R. Plasmon-driven photocatalysis leads to products known from E-beam and X-ray-induced surface chemistry. *Nano Lett.* **18**, 6740–6749 (2018).
- Kontoleta, E. et al. Using hot electrons and hot holes for simultaneous cocatalyst deposition on plasmonic nanostructures. *ACS Appl. Mater. Interfaces* **12**, 35986–35994 (2020).
- Zhou, L. et al. Light-driven methane dry reforming with single atomic site antenna-reactor plasmonic photocatalysts. *Nat. Energy* **5**, 61–70 (2020).
- Kamarudheen, R., Kumari, G. & Baldi, A. Plasmon-driven synthesis of individual metal@semiconductor core@shell nanoparticles. *Nat. Commun.* **11**, 3957 (2020).
- Moreau, A. et al. Controlled-reflectance surfaces with film-coupled colloidal nanoantennas. *Nature* **492**, 86–89 (2012).
- Hövel, H., Fritz, S., Hilger, A., Kreibitz, U. & Vollmer, M. Width of cluster plasmon resonances: bulk dielectric functions and chemical interface damping. *Phys. Rev. B* **48**, 18178–18188 (1993).

34. Zijlstra, P., Paulo, P. M. R., Yu, K., Xu, Q.-H. & Orrit, M. Chemical interface damping in single gold nanorods and its near elimination by tip-specific functionalization. *Angew. Chem. Int. Ed.* **51**, 8352–8355 (2012).
35. Hoggard, A. et al. Using the plasmon linewidth to calculate the time and efficiency of electron transfer between gold nanorods and graphene. *ACS Nano* **7**, 11209–11217 (2013).
36. Lee, S. Y. et al. Tuning chemical interface damping: interfacial electronic effects of adsorbate molecules and sharp tips of single gold bipyramids. *Nano Lett.* **19**, 2568–2574 (2019).
37. Liyanage, T., Nagaraju, M., Johnson, M., Muhoberac, B. B. & Sardar, R. Reversible tuning of the plasmoelectric effect in noble metal nanostructures through manipulation of organic ligand energy levels. *Nano Lett.* **20**, 192–200 (2020).
38. Foerster, B. et al. Chemical interface damping depends on electrons reaching the surface. *ACS Nano* **11**, 2886–2893 (2017).
39. Foerster, B., Spata, V. A., Carter, E. A., Sönnichsen, C. & Link, S. Plasmon damping depends on the chemical nature of the nanoparticle interface. *Sci. Adv.* **5**, eaav0704 (2019).
40. Therrien, A. J. et al. Impact of chemical interface damping on surface plasmon dephasing. *Faraday Discuss.* **214**, 59–72 (2019).
41. Xomalis, A. et al. Controlling optically driven atomic migration using crystal-facet control in plasmonic nanocavities. *ACS Nano* **14**, 10562–10568 (2020).
42. Chikkaraddy, R. et al. How ultranarrow gap symmetries control plasmonic nanocavity modes: from cubes to spheres in the nanoparticle-on-mirror. *ACS Photon.* **4**, 469–475 (2017).
43. Christensen, N. E. & Seraphin, B. O. Relativistic band calculation and the optical properties of gold. *Phys. Rev. B* **4**, 3321–3344 (1971).
44. Moran, C. H., Rycenga, M., Zhang, Q. & Xia, Y. Replacement of poly(vinyl pyrrolidone) by thiols: a systematic study of Ag nanocube functionalization by surface-enhanced Raman scattering. *J. Phys. Chem. C* **115**, 21852–21857 (2011).
45. Linic, S., Chavez, S. & Elias, R. Flow and extraction of energy and charge carriers in hybrid plasmonic nanostructures. *Nat. Mater.* **20**, 916–924 (2021).
46. Negre, C. F. A. & Sánchez, C. G. Effect of molecular adsorbates on the plasmon resonance of metallic nanoparticles. *Chem. Phys. Lett.* **494**, 255–259 (2010).
47. Boerigter, C., Aslam, U. & Linic, S. Mechanism of charge transfer from plasmonic nanostructures to chemically attached materials. *ACS Nano* **10**, 6108–6115 (2016).
48. and, P. A. & Walkup, R. E. Fundamental mechanisms of desorption and fragmentation induced by electronic transitions at surfaces. *Annu. Rev. Phys. Chem.* **40**, 173–206 (1989).
49. Bonn, M. et al. Phonon-versus electron-mediated desorption and oxidation of CO on Ru(0001). *Science* **285**, 1042–1045 (1999).
50. Thomas, A. et al. Tilting a ground-state reactivity landscape by vibrational strong coupling. *Science* **363**, 615–619 (2019).
- Publisher's note** Springer Nature remains neutral with regard to jurisdictional claims in published maps and institutional affiliations.
- © The Author(s), under exclusive licence to Springer Nature Limited 2021

Methods

Electromagnetic simulations. We performed 3D electromagnetic simulations using FDTD software (Lumerical) to obtain the electric-field enhancement profiles in three dimensions and the absorption and scattering cross-section spectra for nanocavities with different spacer thicknesses and nanocube sizes. More details can be found in Supplementary Section 2.

Nanocavity fabrication. Sapphire C plane wafers (Sieget Wafer GmbH) were cut into 12 mm² squares. The samples were sonicated for 10 min in acetone, isopropanol and water. They then underwent mild oxygen plasma descumming (10 s, 50 W; Oxford Instruments-Plasmalab 80+) before a ma-N 1420 (Micro Resist Technology GmbH) negative resist was spin coated on the samples (accelerated at 1,000 r.p.m. s⁻¹ to 4,000 r.p.m., and maintained for 45 s; Suss MicroTec-Delta 80 spin coater). The spin-coated samples were baked at 150 °C for 1 min followed by a 16 s ultraviolet exposure (25 mW cm⁻²; Suss MABA6 UV Mask aligner) through a photolithography mask that contained a grid of numbered squares (100 μm²). The pattern was developed by soaking the samples in Ma-D 533s for 120 s. Next, a chromium adhesion layer (5 nm) and a thick gold layer (100 nm) were deposited (0.05 kÅ rate) in a Polyteknik E-Flex e-beam physical vapour deposition system. After lift-off (10 min in acetone), the patterned gold sample was inserted into a homebuilt atomic layer deposition system and a thin (3–15 nm) Al₂O₃ spacer was deposited with the chamber kept at 1.1 mbar and the stage at 150 °C. Cycles (20–150) of an 18 ms H₂O pulse (milliQ), 18 s delay, 18 ms trimethylaluminum (97%, Sigma-Aldrich) pulse and 18 s delay were executed to achieve a rate of 0.12 nm per cycle (see Supplementary Fig. 2 for TEM images). Then, 20 μl droplets of as purchased gold nanocubes (70 nm sides, citrate capped, 0.05 mg ml⁻¹; Nanopartz) were placed on the sample for 3–4 min, before they were washed away with water and dried with N₂.

Electron microscopy. High-resolution SEM images were acquired using an FEI Verios 460 with an acceleration voltage and current of 5 kV and 100 pA, respectively. Samples were typically imaged at a low magnification (×8,000), high scanning resolution (6,144 × 4,096 pixels) and 3 μs dwell time to generate large area maps with the ability to zoom-in and characterize the shape of individual nanoparticles (Supplementary Fig. 4).

High-resolution TEM images were taken at 200 kV using an FEI Technai G2 F20 X-TWIN TEM. Nanocubes (or colloids) were drop cast on carbon-coated TEM grids to extract the exact dimension of the nanocubes and the spacer's thickness (Supplementary Fig. 2).

Ligand exchange reaction. To exchange the ligands on the gold nanocubes, samples with dropcast citrate-capped nanocubes were placed in a 15 mM solution of MB or a 6 mM solution of NTP for 5 h before rinsing and drying with N₂. MB (Sigma-Aldrich) was in a H₂O (MilliQ) solution and NTP (technical grade, 80%; Sigma-Aldrich) was in anhydrous ethanol (Sigma-Aldrich). Further discussion can be found in Supplementary Section 4.

Raman spectroscopy. Raman spectra were taken in two separate set-ups (with a 633 nm and with a 770 nm laser).

SERS experiments using a 632.8 nm wavelength were obtained with an Olympus BX51 microscope and a motorized and fully automated stage (Prior Scientific H101). A spectrally filtered laser beam at 632.8 nm (Matchbox, Integrated Optics) was focused on the sample with a long working distance, ×100 NA 0.8 objective. Scattered light from the samples was directed into an Andor Shamrock i303 spectrograph and a Newton EMCCD. Typical measurements were done under 22.6 μW μm⁻² and up to 1.2 mW μm⁻² excitation with a 1–10 s collection time, and up to 30 spectra were accumulated to improve the signal-to-noise ratio.

SERS experiments using a 770 nm wavelength were taken with a homebuilt confocal microscopy set-up coupled to a spectrometer (Andor Shamrock A-SR-303i-B-SIL) with a cooled charge-coupled device camera (Andor iVac A-DR324B-FI). Excitation was performed with a narrowband tunable diode laser (New Focus TLB-6712 CW) spectrally cleaned with a pair of bandpass filters (Semrock TBp01-790/12) and directed onto the sample by an Olympus objective (MPlan IR, ×100, NA = 0.95), which was also used for collection. The laser beam was filtered from the collected light with a pair of notch filters (Thorlabs NF785-33), which allowed the detection of both Stokes and anti-Stokes signals. The surface of the sample was imaged with a Basler Ace acA1920-40um camera using a

red-light-emitting diode illumination. Typical measurements were done under 2–100 μW μm⁻² excitation with 1–10 s collection time, and up to 100 spectra were accumulated to improve the signal-to-noise ratio.

Integrating sphere microscopy. The integrating sphere microscopy set-up was designed to allow spatially and spectrally resolved measurements. As a tunable light source, we used a supercontinuum laser (Fianium WL-SC-390-3) sent through an AOTF (Crystal Technologies, approximately 5 nm bandwidth). The incident intensity was controlled with neutral density filters (Thorlabs) and the AOTF radiofrequency power. The incident light was linearly polarized by sending it through a polarizing beam splitter, and a half-wave plate to control the polarization orientation (both Thorlabs). A long working distance objective (Mitutoyo M Apo Plan NIR ×50 NA 0.42 objective with a 17 mm working distance) was used to focus and collect light. The 12 mm² samples were mounted on a 3D piezoelectric stage (Piezajena Tritor400) positioned below a narrow slit of a modified GPS-020-SL integrating sphere (LabSphere). After positioning, the integrated sphere was lowered so that the sample was positioned inside the sphere. For the measurements, we used low-noise Newport 818-UV calibrated photodiodes or Thorlabs PDA100A2 photodetectors, each connected to Stanford Research Systems SR830 lock-in amplifiers. The transmission of the AOTF was digitally modulated with a 50% duty cycle as a source for the lock-in amplifiers. Extinction spectra were obtained by positioning a single NCoM in the focus spot centre and scanning the incoming wavelengths (580–780 nm) with the AOTF (typical measurements were done under ~1.2–2.4 μW μm⁻² illumination). The collected signals were compared with the reflection signal of a bare mirror in an adjacent location (more details in Supplementary Section 3).

Data availability

Datasets generated during and/or analysed during the current study are available online at <https://doi.org/10.6084/m9.figshare.15051894.v1>.

Code availability

All custom codes used in the current study are provided along with the relevant data online at <https://doi.org/10.6084/m9.figshare.15051894.v1>.

Acknowledgements

We thank J. Kuster for software development and support, and L. Leppert and T. B. de Queiroz for helpful discussions. This work was supported by the Dutch Research Council (NWO). I.S., A.X., J.J.B. and A.F.K. acknowledge support from the European Research Council (ERC) under the Horizon 2020 Research and Innovation Programme THOR (grant agreement no. 829067), PICOFORCE (grant agreement no. 883703) and POSEIDON (grant agreement no. 861950). J.J.B. acknowledges funding from the EPSRC (Cambridge NanoDTC EP/L015978/1, EP/L027151/1, EP/S022953/1, EP/P029426/1 and EP/R020965/1). A.B. acknowledges support from the Dutch Research Council (NWO) via the Vidi award 680-47-550.

Author contributions

E.C.G., E.O. and A.B. conceived the experiments. I.S., A.X., J.J.B. and A.F.K. performed the SERS measurements. E.O. fabricated the samples, performed the optical measurement, conducted the electromagnetic simulations, produced the electron microscopy images and analysed the data. E.C.G. and E.O. wrote the manuscript. All the authors discussed the results and commented on the manuscript.

Competing interests

The authors declare no competing interests.

Additional information

Supplementary information The online version contains supplementary material available at <https://doi.org/10.1038/s41565-021-00973-6>.

Correspondence and requests for materials should be addressed to Erik C. Garnett.

Peer review information *Nature Nanotechnology* thanks Suljo Linic and the other, anonymous, reviewer(s) for their contribution to the peer review of this work.

Reprints and permissions information is available at www.nature.com/reprints.